AIChE

# Particle Surface Temperature Measurements with Multicolor Band Pyrometry

**Hong Lu, Leong-Teng Ip, Andrew Mackrory, Luke Werrett, Justin Scott, Dale Tree, and Larry Baxter**
Chemical Engineering Dept., Brigham Young University, Provo, UT 84602

*DOI 10.1002/aic.11677*
*Published online November 10, 2008 in Wiley InterScience (www.interscience.wiley.com).*

*A noncontact, color-band pyrometer, based on widely available, inexpensive digital imaging devices, such as commercial color cameras, and capable of pixel-by-pixel resolution of particle-surface temperature and emissivity is demonstrated and described. This diagnostic instrument is ideally suited to many combustion environments. The devices used in this method include color charge-coupled device (CCD), or complementary metal oxide semiconductor (CMOS) digital camera, or any other color-rendering camera. The color camera provides spectrally resolved light intensity data of the image, most commonly for three color bands (Red, Green, and Blue,), but in some cases for four or more bands or for a different set of colors. The CCD or CMOS sensor-mask combination has a specific spectral response curve for each of these color bands that spans the visible and often near infrared spectral range. A theory is developed, based on radiative heat transfer and camera responsivity that allows quantitative surface temperature distribution calculation, based on a photograph of an object in emitted light. Particle surface temperature calculation is corrected by heat transfer analysis with reflection between the particle and reactor wall for particles located in furnace environments, but such corrections lead to useful results only when the particle temperature is near or below the wall temperatures. Wood particle-surface temperatures were measured with this color-band pyrometry during pyrolysis and combustion processes, which agree well with thermocouple measured data. Particle-surface temperature data simultaneously measured from three orthogonal directions were also mapped onto the surface of a computer generated 3-D (three-dimensional) particle model.* © 2008 American Institute of Chemical Engineers *AIChE J,* 55: 243–255, 2009
*Keywords: color-band, pyrometry, particle, surface, temperature, measurement*

## Introduction

Particle temperature determines reaction rates and product distributions and yields, and, hence, is a critical combustion parameter. Optical pyrometry[1–6] is an established, noncontact temperature measurement technique for solid fuel particles, soot particles, and flames. Traditional pyrometry consists of isolating narrow spectral line intensities with narrow band filters and recording signal intensities on, for example, photon multiplier tubes. Line intensity at a single wavelength can be used to estimate temperature if the surface emissivity, emitting area, and optical and system parameters are known. Line intensities at two or more wavelengths can eliminate the need to know the surface emissivities (so long as they are the same at each wavelength), emitting areas, etc., in a technique commonly called two-color or multicolor pyrometry. A digital color image offers the potential to extend this technique to obtain pixel-by-pixel temperature and emissivity measurements, with the rapid commercialization of such cameras

Correspondence concerning this article should be addressed to H. Lu at honglu@research.ge.com.

driving prices down and performance up such that inexpensive and highly capable systems can be built on current technologies. Such digital images spectrally resolve light into broad bands,[7–8] as opposed to narrow lines more traditionally associated with pyrometry. However, mathematical algorithms that are conceptually similar to the multicolor (and one-color) techniques traditionally used in pyrometry render such images highly accurate and relatively sensitive measures of particle temperature. We call this technique and algorithm color-band pyrometry to distinguish it from traditional pyrometry methods.

## Color-Band Pyrometry Algorith Development

### *Color-band pyrometry principles*

Blackbody spectral radiance expressed as $B_\lambda^b = C_1\lambda^5/(e^{C_2/\lambda T} - 1)$, forms the basis of Planck's law. For a gray body: $B_\lambda = \varepsilon_\lambda B_\lambda^b$, where $\varepsilon(\lambda)$ is the spectral emissivity. The total radiance is $B = \int_0^\infty B_\lambda d\lambda$. In the wavelength range between $\lambda_1$ and $\lambda_2$, the total radiance is $B = \int_{\lambda_1}^{\lambda_2} B_\lambda d\lambda$. For a typical pyrometer illustrated in Figure 1 (where, the point light source dimension is much smaller than the distance $d$ from the source to the receptor - lens, and $d \gg D$ is usually true for most applications), the solid angle is $\Omega = \pi D^2/4d^2$, where $D$ is the lens (receptor) diameter, and $d$ is the working distance between the lens and the point light source.

Assuming the total effective extended source area is $A_1$, the spectral radiant power and total radiant power incident on the lens are $\Phi_{i,\lambda} = B_\lambda A_1 \pi D^2/4d^2$, and $\Phi_i = BA_1\pi D^2/4d^2$, respectively.

If the transmittance (which is the is the ratio of the total radiant or luminous flux transmitted by a transparent object to the incident flux, usually given for normal incidence) of the optical system is $\tau_\lambda$, the spectral energy incident on the imaging sensor will be $\Phi_{i,\lambda,\text{sensor}} = B_\lambda \tau_\lambda A_1 \pi D^2/4d^2$. With an effective image area of $\boldsymbol{A_2}$ on the imaging sensor, which corresponds to the effective extended light source area, and a pixel/cell area of $a$ on the CCD or CMOS sensor, the spectral irradiance obtained by a specific pixel/cell is $E_\lambda = B_\lambda \tau_\lambda a A_1 \pi D^2/4d^2 A_2$. Generally, $\boldsymbol{A_2/A_1}$ is proportional to the magnification factor of the lens, and here we can use $\boldsymbol{X}$ to replace it.

Usually there are two methods to describe the spectral sensitivity/responsivity $\boldsymbol{S_\lambda}$, of an imaging sensor. One is quantum efficiency (QE, electrons/photon), which is the photon-to-electron conversion efficiency; the other one uses the energy to electron conversion efficiency. In addition, the electron to digital number (pixel intensity) conversion is related the gain value of the CCD or CMOS camera.

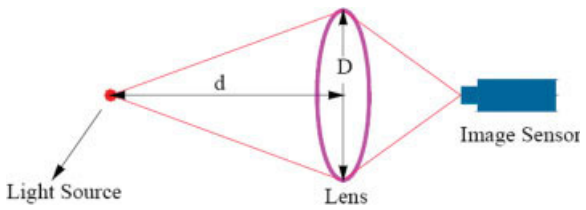


**Figure 1. Schematic diagram of the color-band pyrometry.**

[Color figure can be viewed in the online issue, which is available at www.interscience.wiley.com.]

The energy of a photon as a function of frequency or wavelength is $\boldsymbol{E} = \boldsymbol{hc}/\lambda$. If QE is used as the spectral sensitivity/responsivity, with an exposure time of $\Delta\boldsymbol{t}$, the digital number ($DN$) or pixel intensity of any pixel in the image is calculated by Eq. 1 for an ideally performing (perfectly linear) black-and-white CCD or CMOS camera based on the optical system and camera characteristics illustrated earlier.

$$DN = \alpha \cdot \frac{\pi}{4} \cdot \left(\frac{D}{d}\right)^2 \cdot f(g) \cdot \frac{a}{X} \cdot \Delta t \cdot \int_{\lambda_1}^{\lambda_2} \varepsilon_\lambda \tau_\lambda S_\lambda \cdot \frac{C_1 \cdot \lambda^{-5}}{e^{C_2/\lambda \cdot T} - 1} \cdot \left(\frac{h \cdot c}{\lambda}\right)^{-1} \cdot d\lambda, \quad (1)$$

where, $\alpha$ is a proportional factor that ensures the units consistent for the equation, and $f(g)$ is a function of gain value of the camera; all other variables are explained earlier and in the notation section.

The spectral radiances of the object surface from the lowest wavelength to the highest wavelength that can be detected by the image sensor all contribute to the pixel intensity, by contrast to only two narrow wavelengths in traditional two-color pyrometry. This dramatically increased the signal strength.

If the spectral responsivity uses the energy to electron conversion efficiency, $(h \cdot c/\lambda)^{-1}$ needs to be removed from the aforementioned equation, as shown in Eq. 2. This equation can be simplified if spectral emissivity is independent of wavelength

$$DN = \alpha \cdot \frac{\pi}{4} \cdot \left(\frac{D}{d}\right)^2 \cdot f(g) \cdot \frac{a}{X} \cdot \Delta t \cdot \int_{\lambda_1}^{\lambda_2} \varepsilon_\lambda T_\lambda S_\lambda \cdot \frac{C_1 \cdot \lambda^{-5}}{e^{C_2/\lambda \cdot T} - 1} d\lambda \quad (2)$$

By far the most common method of rendering color images in commercial digital cameras involves creating a color filter mosaic array (CFA) on top of a light intensity (black-and-white) imager. In most cases, a 3-color, red-green-blue (RGB) pattern appears in the CFA, although there are other options, including 3-color complementary YeMaCy arrays, mixed primary/complementary colors, and 4-color systems where the fourth color is white or a color with shifted spectral sensitivity. One manufacturer (Foveon) uses a system that separates color based on penetration depth of the signal in the silicon detector with no mosaic filter.

A Bayer filter mosaic, as shown in Figure 2, represents the most commonly used CFA for arranging RGB color filters on a square grid of photo sensors. This term comes from the name of its inventor, Bryce Bayer of Eastman Kodak, and refers to the particular arrangement of color filters used in most single-chip digital cameras. Bryce Bayer's patent called the green photo sensors luminance-sensitive elements, and the red and blue ones chrominance-sensitive elements. He used twice as many green elements as red or blue to mimic the human eye's greater resolving power with green light. He referred to these elements as samples and after interpolation they become pixels.

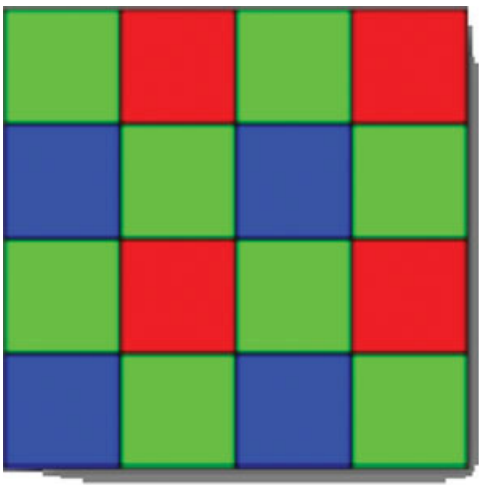

**Figure 2. Bayer filter color pattern.**

[Color figure can be viewed in the online issue, which is available at www.interscience.wiley.com.]

There are a number of different ways the pixels are arranged in practice, but the pattern shown in Figure 2 with alternating values of red (R), and green (G), for odd rows and alternating values of green (G), and blue (B), for even rows is very common. The raw output of Bayer-filter cameras is referred to as a Bayer Pattern image. Since each pixel records only one of the three colors, two-thirds of the color data are missing from each, as illustrated in Figure 3. The green is usually read out as two separate fields, or as one field with twice as many points.

A demosaicing algorithm interpolates a complete RGB set for each point and produces the RGB image. Many different algorithms exist, and they are one of the distinguishing factors in commercial cameras that otherwise often use the same sensors. The simplest is the bilinear interpolation method. In this method, the red value of a non red pixel is computed as the average of the adjacent red pixels, and similar for blue and green.

With the Bayer filter in front of the CCD or CMOS sensor, sensor spectral responsivity can be measured for each individual color. As a result, the pixel intensity (or digital number) of the red color/channel is correlated with object temperature and red color/channel spectral responsivity as shown in Eq. 3, and similarly for the other two colors/channels

$$DN_{\mathrm{Red}} = \alpha \cdot \frac{\pi}{4} \cdot \left(\frac{D}{d}\right)^2 \cdot f(g_{\mathrm{Red}}) \cdot \frac{a}{X} \cdot \Delta t \cdot \int_{\lambda_1}^{\lambda_2} \varepsilon_\lambda \tau_\lambda S_{\lambda,\mathrm{Red}} \cdot \frac{C_1 \cdot \lambda^{-5}}{e^{C_2/\lambda \cdot T} - 1} d\lambda \quad (3)$$

Occasionally, a manufacturer provides the color or black-and-white spectral responsivity of CCD or CMOS cameras. To calculate the object surface temperature, Eq. 3 applies to each color (typically RGB) channels. Assuming both spectral emissivity and spectral transmission are independent of wavelength and setting the gain value of each color to be the same, a new equation with only one (implicit) unknown — the temperature — results, as shown in Eq. 4. This is the basic equation for the color-band method. Any two of the three channels/colors can be used to calculate the object surface temperature based on the pixel intensity of each color. This technique is flexible. The camera does not have to be focused on the surface of the object for a reliable temperature, although it does have to be focused for reliable spatial distributions of temperature and, in all cases, only pixels with light that originates from the surface are valid pixels for temperature measurement. Images with poor focus contain many pixels with mixed particle-background light. In addition, working distance, lens aperture size, and exposure time all provide additional adjustable parameters that impact signal level. It is not necessary to measure working distance and aperture size. Only exposure time might be needed, which can be controlled and read through the camera control software

$$\frac{DN_{\mathrm{Blue}}}{DN_{\mathrm{Red}}} = \frac{\int_{\lambda_1}^{\lambda_2} S_{\lambda,\mathrm{Blue}} \cdot \frac{C_1 \cdot \lambda^{-5}}{e^{C_2/\lambda \cdot T} - 1} d\lambda}{\int_{\lambda_1}^{\lambda_2} S_{\lambda,\mathrm{Red}} \cdot \frac{C_1 \cdot \lambda^{-5}}{e^{C_2/\lambda \cdot T} - 1} d\lambda} \quad (4)$$

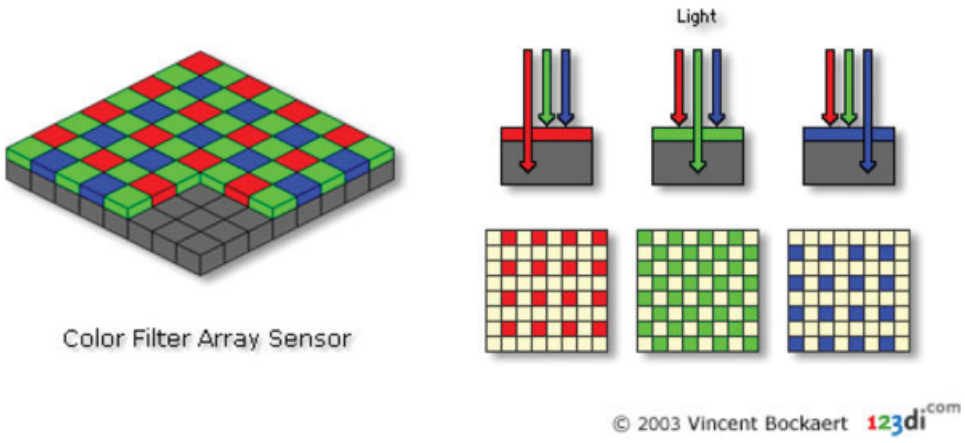


**Figure 3. Color image reconstruction from a Bayer filter.[9]**

[Color figure can be viewed in the online issue, which is available at www.interscience.wiley.com.]

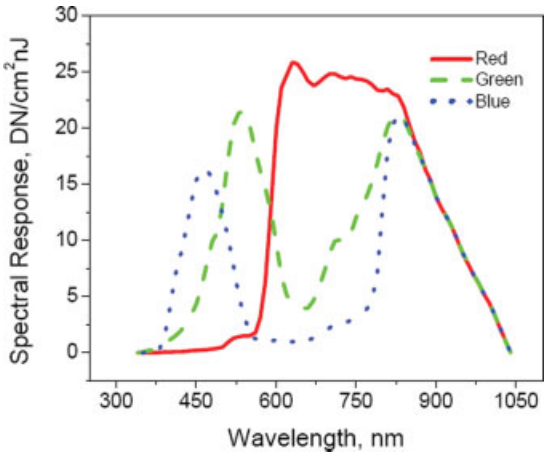


**Figure 4. Spectral responsivity of the ZR32112 CMOS sensor.[10]**

[Color figure can be viewed in the online issue, which is available at www.interscience.wiley.com.]

### *CMOS-camera-based color-band pyrometry*

In this project, a CMOS camera from EPIX, Inc. (model SV2112) was first used to measure blackbody temperature (Mikron Model M330). The camera uses a PixelCam™ ZR32112 CMOS sensor. Spectral responsivities of each color/channel, as well as the monochrome, appear in Figure 4. The IR filter in front of the CMOS sensor in the camera was removed to obtain maximum response from the camera since near-infrared signal is critical at low-temperature measurements, as indicated by Planck's law.

Using the spectral responsivity curves obtained from the manufacture and without calibrating the SV2112 CMOS camera, temperatures of a blackbody were measured by both a type-K thermocouple and the CMOS camera. The XCAP image acquisition and process software provided Pixel intensity of each color. The junction-compensated-thermocouple data compared with the camera measurements appear in Figure 5.

When the blackbody temperature was higher than 900 K, the differences between the camera-measured temperature data and the thermocouple results were less than 50 K. Due to the spectral responsivity similarity of the three colors/channels in the near IR range ($\lambda > 800$ nm) where low-temperature radiation dominates, the camera measurements differ by more than 100 K from the blackbody temperature and are scattered at temperatures below 900 K. Figure 6 illustrates this issue, the data for which are based on Eq. 4. When the blackbody temperature is lower than 900 K, the pixel intensity ratio of any two colors/channels approaches 1.0 making accurate temperature measurement difficult. If the near infrared spectral response of the camera were blocked by a near IR filter, as is usually done in commercial cameras (we removed the filter in this camera), the pixel intensity ratio as a function of temperature would remain high, but the total signal would decrease dramatically. In such cases, larger apertures, longer exposure times, or more sensitive detectors would be required to obtain useful data at low-temperatures.

CMOS sensors reportedly exhibit a slightly higher spectral responsivity than CCD sensors, especially at the near infrared (NIR) range. However, CCD sensors commonly perform better than CMOS sensors with respect to uniformity, signal-to-noise ratio, and dynamic range. The low to moderate uniformity and signal-to-noise ratio may also contribute to the inaccuracy of temperature measurement of the SV2112 COMS camera at the low-temperature range.

To obtain better temperature measurement results, a CCD camera was also used in this project.

### *CCD-camera-based color-band pyrometry*

The SVS285CLCS camera uses a Sony Exview HAD CCD, which has very high-sensitivity and low-smear. This sensor shows higher sensitivity at the NIR range than traditional CCDs due to the Exview HAD CCD technology. Similar to the CMOS camera, the IR filter was removed from the camera to maximize signal. The available spectral responsivity graph from the manufacturer appears in Figure 7, which only displays the visible spectral range.

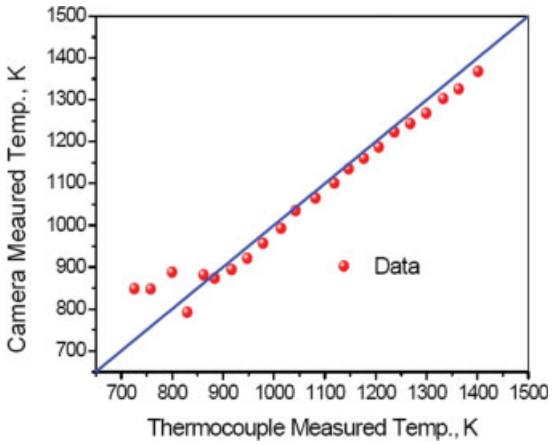


**Figure 5. Temperature comparison of thermocouple and CMOS camera measurements.**

[Color figure can be viewed in the online issue, which is available at www.interscience.wiley.com.]

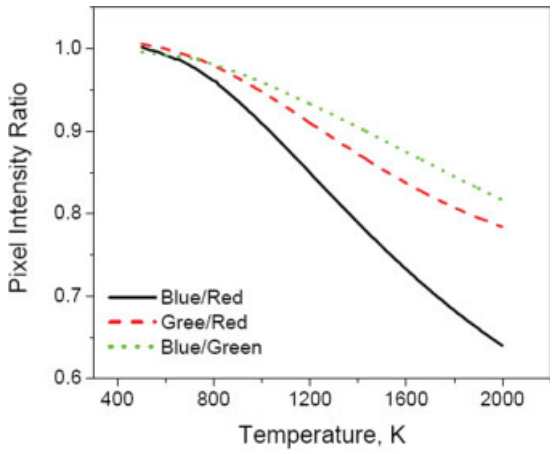


**Figure 6. CMOS camera pixel intensity ratios as functions of temperature.**

[Color figure can be viewed in the online issue, which is available at www.interscience.wiley.com.]

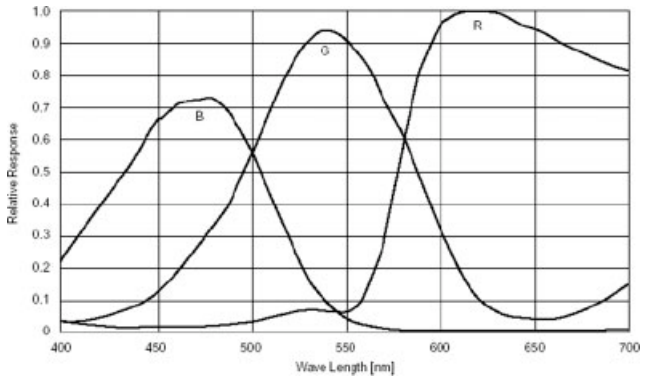


**Figure 7. Manufacturer provided ICX285AQ CCD sensor spectral responsivity.[11]**

The complete spectral responsivity of each color/channel was measured with a blackbody as light source, and a monochromator (CornerStone 130) separating the broad-band light into narrow-wavelength signals with a resolution of 0.5 nm. The blackbody temperature was set to 1,600 °C to maximize the signal/noise ratio. The measured wavelength range is from 300 nm to 1,150 nm. A high-pass filter (LPF750 Lot NNB) placed between the camera and the outlet of the monochromator blocked the second- and higher-order diffractions when measuring wavelengths longer than 750 nm. Both the spectral efficiency of the monochromator and the transmission efficiency of the filter impact the calculation of the spectral responsivity of the CCD sensor. Energy carried by a specific wavelength signal was calculated by Planck's law. The mathematical calculation of spectral responsivity for each color/channel appears as Eq. 5

$$S_{\lambda,\text{color}} = \frac{DN_{\text{color},\lambda}}{\tau_{\text{filter},\lambda}\ \ \xi_{\text{mono},\lambda} \cdot \frac{C_1\ \lambda^5}{e^{C_2/\lambda T_B} - 1}} \tag{5}$$

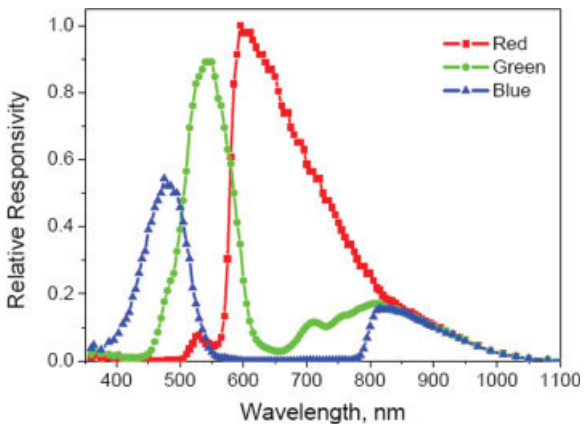


**Figure 8. Measured relative spectral responsivity of the SVS285CSCL camera.**

[Color figure can be viewed in the online issue, which is available at www.interscience.wiley.com.]

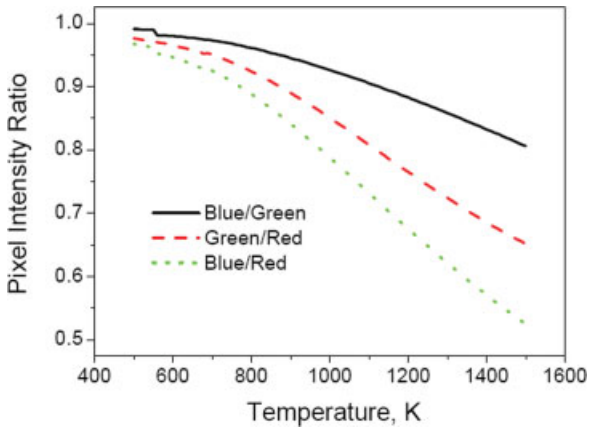


**Figure 9. CCD camera pixel intensity ratios as functions of temperature.**

[Color figure can be viewed in the online issue, which is available at www.interscience.wiley.com.]

where, ***color*** = Red, Green, and Blue. $\tau_{\text{filter},\lambda}$ is the transmittance of the high-pass filter, $\xi_{\text{mono},\lambda}$ is the spectral efficiency of the monochromator, $DN_{\text{color},\lambda}$ is the digital number or pixel intensity of each color at $\lambda$.

A complete relative spectral responsivity of each color/channel normalized by the maximum value, which occurred in the red color/channel, appears in Figure 8. The measured spectral responsivity curves of the CCD camera have similar shapes as those obtained from the manufacturer for the CCD sensor, but include the near IR region. The small differences may arise from sample-to-sample variations in the sensors (manufacturer's data are typical, but not obtained on each sensor), the camera characteristics, and the transmittance of the camera lens.

With the measured relative spectral responsivity curves, the pixel intensity ratios of any two colors/channels appear in Figure 9. The ratio of blue to red depends more strongly on temperature than the other two ratio values, as would be

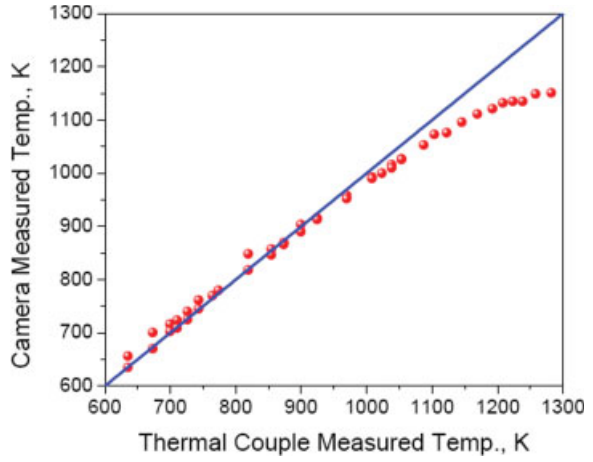


**Figure 10. Temperature comparison of thermocouple and CCD camera measurements.**

[Color figure can be viewed in the online issue, which is available at www.interscience.wiley.com.]

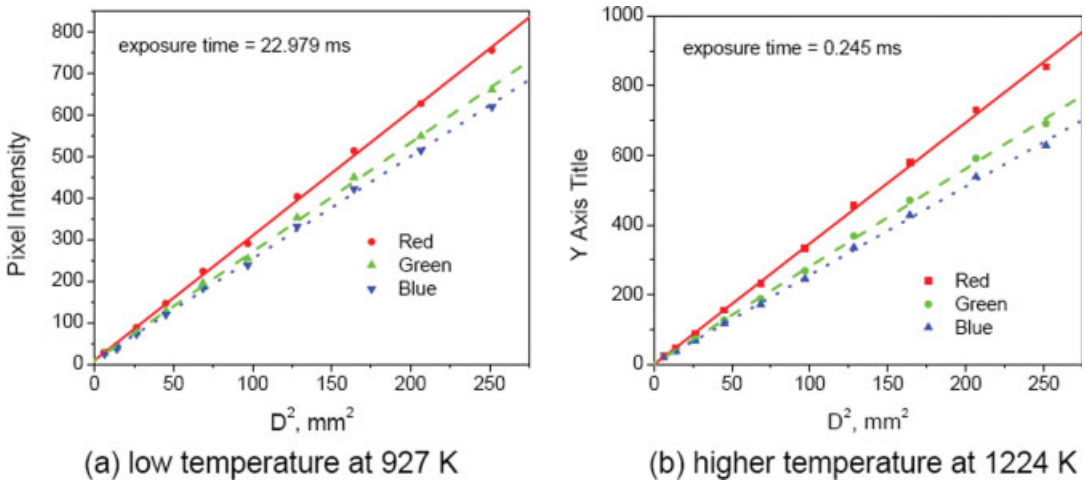


**Figure 11. Pixel intensity vs. effective aperture area.**

[Color figure can be viewed in the online issue, which is available at www.interscience.wiley.com.]

expected since they differ the greatest in average wavelength. This ratio should result in the most sensitive/accurate temperature measurement.

Figure 9 shows that the CCD camera is able to measure a wider temperature range compared with the CMOS camera since the CCD camera pixel intensity ratios approach 1.0 at lower-temperature (~650 K). The blackbody temperatures were then measured with this CCD camera, and calculated using Eq. 4 and the complete spectral responsivities. The camera-measured data compared with thermocouple measurements appear in Figure 10, again without calibration. The results show that the CCD camera measurements were within 50 K of the thermocouple measured values when blackbody temperature is lower than 1,050 K, but the sensor appears to begin to saturate at higher-temperatures. Further calibration is necessary for more accurate and wider temperature range measurements.

To calibrate the CCD camera and make this method more robust, four variables were studied: the square of lens aperture size divided by the square of the working distance $\boldsymbol{D}^2/d^2$; exposure time $\Delta t$; blackbody temperature $T$; and camera gain value $g$.

The first investigation explored the linearity implied by Eq. 2 between the pixel intensity and $\boldsymbol{D}^2/d^2$. Aperture size adjustments produced image pixel intensity data as a function of $\boldsymbol{D}^2$ at a variety of temperatures and exposure times. Results indicated an almost perfectly linearity in all cases (Figure 11). Here only two cases appear: low-temperature and long exposure time data appear in Figure 11a, and high-temperature and short exposure time data appear in Figure 11b. In the calibration, working distance remained constant and only aperture size changed since $\boldsymbol{D}^2$ and $1/\boldsymbol{d}^2$ should have identical effects.

The camera gain value function $\boldsymbol{f}$ ($\boldsymbol{g}$), was calibrated for each channel at different temperatures and exposure times. For each channel at any condition, the gain value function $\boldsymbol{f}$ ($\boldsymbol{g}$), followed the form of $e^{y \cdot g}$, as shown in Figure 12. The parameter in this function is almost constant, so an average value was calculated for each channel: 3.424, 3.424, and 3.428, respectively, for red, green, and blue channels. They can be treated as the same for each channel to simplify the color-band method.

When blackbody temperatures exceeded about 850 K, the image pixel intensity was nearly proportional to exposure time, but both the slope and intercept of the straight line started to increase with increasing blackbody temperature, as shown in Figure 13. The green and blue channel behaved similarly, and only the red channel appears here. These data follow a linear correlation, but with a nonzero intercept (Eq. 6), between the pixel intensity and exposure time when blackbody temperature is higher than 850 K. Both the slope and intercept are functions of the energy received by the CCD camera sensor, increasing with blackbody temperature increase. These effects presumably arise from pixel saturation as the signal nears the upper limits of the pixel dynamic range

$$DN_{\mathrm{Red}} = a_{\mathrm{Red}}(E_{\mathrm{Red}})\Delta t + b_{\mathrm{Red}}(E_{\mathrm{Red}}) \tag{6}$$

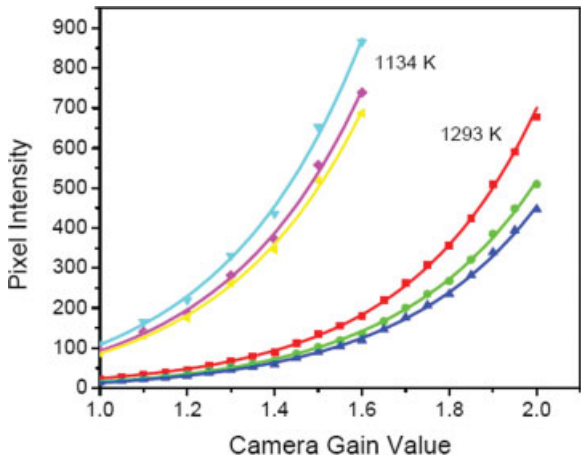


**Figure 12. Camera gain value calibration.**

[Color figure can be viewed in the online issue, which is available at www.interscience.wiley.com.]

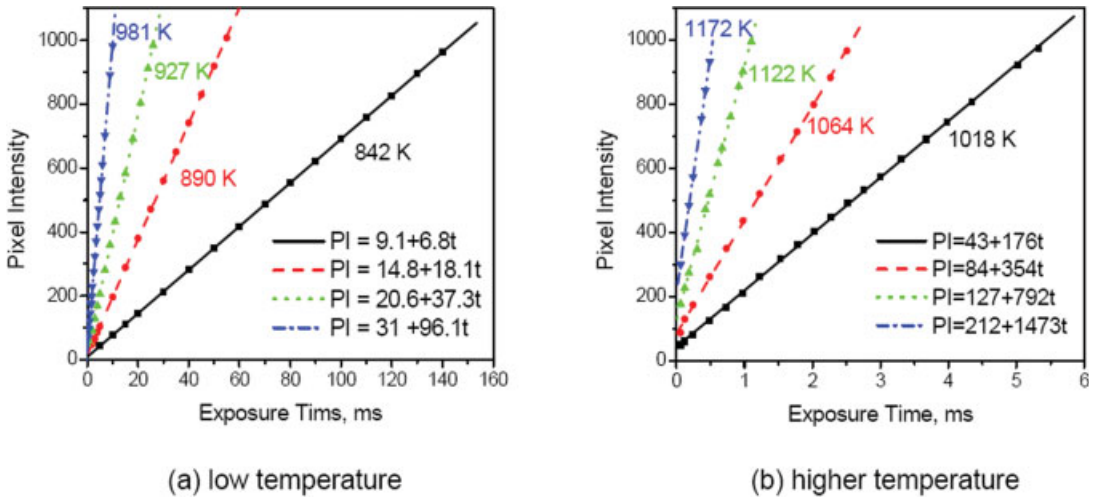


**Figure 13. Red channel pixel intensity vs. exposure time at different temperature.**

[Color figure can be viewed in the online issue, which is available at www.interscience.wiley.com.]

where

$$E_{\mathrm{Red}} = \int_{\lambda_1}^{\lambda_2} S_{\lambda,\mathrm{Red}} \cdot \frac{C_1 \cdot \lambda^{-5}}{e^{C_2/\lambda \cdot T} - 1} d\lambda$$

To determine the exact relation between the energy and slope, as well as that between the energy and intercept, blackbody temperature was changed from about 850 K to 1312 K in increments of about 80 K. The slope and intercept in Eq. 6 were calculated by adjusting the exposure time at each temperature. Both slope and intercept fit power functions of the energy, as shown in Figure 14. The camera was also calibrated at higher temperature range (>1,273 K) with a high-power blackbody. The fitted functions were slightly different from what fitted for moderate temperature range, as shown in Figure 15.

The final calibrations appear as Eq. 7 for moderate- and Eq. 8 for high-temperature ranges. The simplest form, Eq. 3, reliably computes low-temperature results by the color-band method

$$\begin{aligned} DN_{\mathrm{Red}} &= \alpha \cdot \left(\frac{D}{d}\right)^2 \cdot e^{3.424 \cdot g} \cdot (\Delta t \cdot 280 \cdot E_{\mathrm{Red}}(T)^{0.958} \\ &\quad + 60.5 \cdot E_{\mathrm{Red}}(T)^{0.80}) \\ DN_{\mathrm{Green}} &= \alpha \cdot \left(\frac{D}{d}\right)^2 \cdot e^{3.424 \cdot g} \cdot (\Delta t \cdot 272 \cdot E_{\mathrm{Green}}(T)^{0.959} \\ &\quad + 63.4 \cdot E_{\mathrm{Green}}(T)^{0.86}) \\ DN_{\mathrm{Blue}} &= \alpha \cdot \left(\frac{D}{d}\right)^2 \cdot e^{3.428 \cdot g} \cdot (\Delta t \cdot 272 \cdot E_{\mathrm{Blue}}(T)^{0.955} \\ &\quad + 65 \cdot E_{\mathrm{Blue}}(T)^{0.87}) \end{aligned} \tag{7}$$

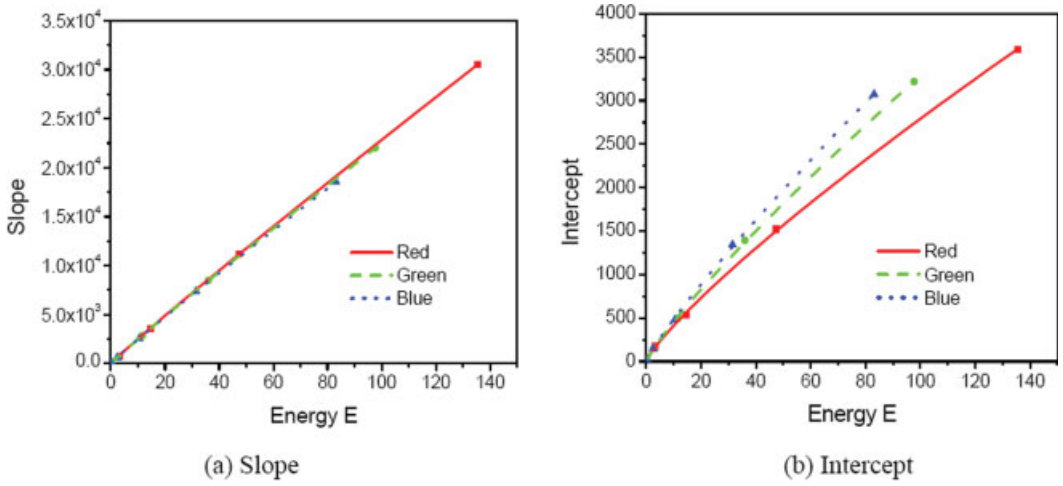


**Figure 14. Slope and intercept vs. energy at moderate temperature range.**

[Color figure can be viewed in the online issue, which is available at www.interscience.wiley.com.]

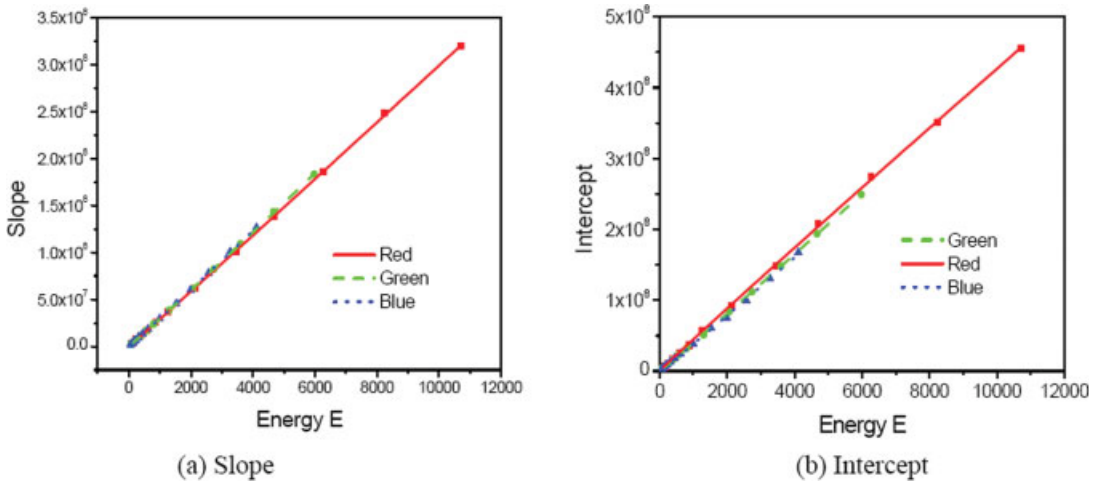


**Figure 15. Slope and intercept vs. energy at higher-temperature range (>1,273 K).**

[Color figure can be viewed in the online issue, which is available at www.interscience.wiley.com.]

$$DN_{\mathrm{Red}} = \alpha \cdot \left(\frac{D}{d}\right)^2 \cdot e^{3.424.g} \cdot (\Delta t \cdot 264 \cdot E_{\mathrm{Red}}(T)^{1.013} + 526 \cdot E_{\mathrm{Red}}(T)^{0.977})$$

$$DN_{\mathrm{Green}} = \alpha \cdot \left(\frac{D}{d}\right)^2 \cdot e^{3.424.g} \cdot (\Delta t \cdot 254 \cdot E_{\mathrm{Green}}(T)^{1.022} + 344 \cdot E_{\mathrm{Green}}(T)^{1.022})$$

$$DN_{\mathrm{Blue}} = \alpha \cdot \left(\frac{D}{d}\right)^2 \cdot e^{3.428.g} \cdot (\Delta t \cdot 252 \cdot E_{\mathrm{Blue}}(T)^{1.024} + 307 \cdot E_{\mathrm{Blue}}(T)^{1.032}) \quad (8)$$

If the CCD sensor spectral responsivities were measured accurately enough, all three colors/channels of the camera should have the same digital number vs. energy correlation. The discrepancy might be introduced by the errors in spectral responsivity measurements.

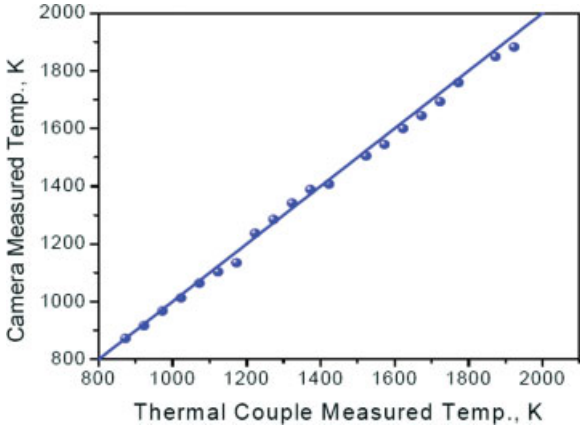


**Figure 16. Blackbody temperature measured by the calibrated CCD camera.**

[Color figure can be viewed in the online issue, which is available at www.interscience.wiley.com.]

Both Figures 14 and 15, as well as Eqs. 7 and 8, show that the slope and intercept become more linear with respect to the received energy when blackbody temperature increases. With the equations obtained, the blackbody temperature was measured by the color-band method at random working distance and random exposure time. Results compared with thermocouple data appear in Figure 16. The error is within 3%.

### *Particle temperature measurements correction for reflection effects in furnace*

If the particle is heated in a furnace and the furnace wall temperature differs from the particle surface temperature, the measurement has to be corrected by taking surface reflection effects into account.

To simplify the correction, the following assumptions were made:

- The wall temperature and surface properties are uniform;
- All energy is emitted and reflected diffusely;
- Both the particle and the wall surfaces are gray;
- The particle surface is convex;
- The incident, and, hence, reflected energy flux is uniform over the surface area;

The reactor is an enclosure and the particle is located in the center of the reactor.

Based on the aforementioned assumptions, a heat-transfer diagram between the particle and the wall surface appears in Figure 17. The surface areas are $A_1$, $A_2$, and $A_v$ for particle, reactor, and the view port hole, respectively. Particle surface temperature is $T_1$ and $T_2$ designates the reactor wall. It is also assumed that the surface areas of the particle and the view port are much less than that of the reactor wall: $A_1 \ll A_2$ and $A_v \ll A_2$.

Geometric configuration factors[12] of the particle surface and the reactor surface are $\boldsymbol{F}_{1\text{-}1}$, $\boldsymbol{F}_{1\text{-}2}$, $\boldsymbol{F}_{2\text{-}1}$ and $\boldsymbol{F}_{2\text{-}2}$. By analyzing the radiant energy interchange between the particle surface and the reactor wall, the radiant energy flux leaving

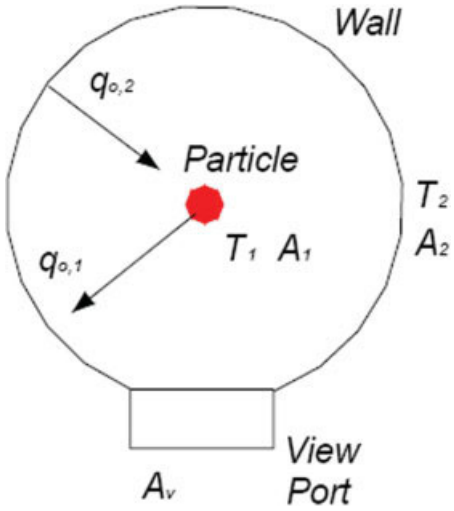


**Figure 17. Radiant heat interchange between particle and reactor wall.**

[Color figure can be viewed in the online issue, which is available at www.interscience.wiley.com.]

the particle surface $\boldsymbol{q}_{o,1}$, and that leaving the reactor wall surface $\boldsymbol{q}_{o,2}$ were developed, as shown in Eqs. 9 and 10

$$q_{o,1} = \varepsilon_1 \sigma T_1^4 + (1-\varepsilon_1)(F_{1-1}q_{o,1} + F_{1-2}q_{o,2}) \tag{9}$$

$$q_{o,2} = \varepsilon_2 \sigma T_2^4 + (1-\varepsilon_2)(F_{2-1}q_{o,1} + F_{2-2}q_{o,2}) \tag{10}$$

Substituting Eq. 10 into Eq. 9 results in Eq. 11

$$q_{o,1} = \frac{[1-(1-\varepsilon_2)F_{2-2}]\varepsilon_1 \sigma T_1^4 + (1-\varepsilon_1)\varepsilon_2 \sigma T_2^4}{[1-(1-\varepsilon_2)F_{2-2}] + [(1-\varepsilon_1)(1-\varepsilon_2)F_{2-1}]} \tag{11}$$

The aforementioned equation can be simplified for this system. The assumption of convex particle surface leads to $\boldsymbol{F}_{1\text{-}1} = 0$, and $\boldsymbol{F}_{1\text{-}2} =$ since $\boldsymbol{F}_{1\text{-}1} + \boldsymbol{F}_{1\text{-}2} = 1$. According to the reciprocity relation between any two radiant elements $\boldsymbol{F}_{1\text{-}2} \cdot A_1 = \boldsymbol{F}_{2\text{-}1} \cdot A_2$, the radiant energy leaving the reactor wall that arrives the particle surface is $\boldsymbol{F}_{2\text{-}1} = A_1/A_2$. Similarly, it is straightforward to get $F_{2-2} = 1 - A_1/A_2$. So, $\boldsymbol{F}_{2\text{-}1} = 0$ and $\boldsymbol{F}_{2\text{-}2} = 1$ since $A_1 \ll A_2$. Equation 11 then simplifies to Eq. 12. Equation 11 also simplifies to Equation 12 if the emissivity of the reactor wall is 1.0.

$$q_{o,1} = \varepsilon_1 \sigma T_1^4 + (1-\varepsilon_1)\sigma T_2^4 \tag{12}$$

Similarly, the spectral radiant energy flux leaving the particle surface appears as Eq. 13

$$q_{o,1,\lambda} = \varepsilon_1 \frac{C_1 \cdot \lambda^{-5}}{e^{C_2/\lambda \cdot T_1} - 1} + (1-\varepsilon_1)\frac{C_1 \cdot \lambda^{-5}}{e^{C_2/\lambda \cdot T_2} - 1} \tag{13}$$

For color-band pyrometry with Eq. 4, the corrected equation results from replacing the Planck's radiant energy with Eq. 13. The result appears in Eq. 14.

$$\frac{DN_{\text{Blue}}}{DN_{\text{Red}}} = \frac{\int_{\lambda_1}^{\lambda_2} S_{\lambda,\text{Blue}} \cdot \left(\varepsilon_1 \frac{C_1 \cdot \lambda^{-5}}{e^{C_2/\lambda \cdot T_1} - 1} + (1-\varepsilon_1)\frac{C_1 \cdot \lambda^{-5}}{e^{C_2/\lambda \cdot T_2} - 1}\right) d\lambda}{\int_{\lambda_1}^{\lambda_2} S_{\lambda,\text{Red}} \cdot \left(\varepsilon_1 \frac{C_1 \cdot \lambda^{-5}}{e^{C_2/\lambda \cdot T_1} - 1} + (1-\varepsilon_1)\frac{C_1 \cdot \lambda^{-5}}{e^{C_2/\lambda \cdot T_2} - 1}\right) d\lambda} \tag{14}$$

Similar equation can be established for any other two channel combinations: blue/green or green/red, and both particle emissivity and particle surface temperature can be obtained simultaneously.

## Results and Discussion

With the calibrated multicolor band pyrometer, solid-particle-surface temperature and flame temperature can be measured during particle devolatilization and char burning processes in a single-particle reactor, and an entrained-flow reactor. Examples of temperatures for several burning particles of various fuel type and size appear below. In the single-particle reactor, 11 mm poplar particles suspended in the center of the single-particle reactor provide most of the data. Particle-surface temperatures were also measured with a thermocouple embedded in a shallow groove opened on the particle surface. Small-size sawdust particles (~0.3 mm) were used in the entrained flow reactor. Both the single-particle reactor and the entrained-flow reactor have optical access from three orthogonal directions, so that the particle-surface temperature can be measured simultaneously from different angles with three CCD camera color-band pyrometers.

### *Particle-surface temperature during devolatilization*

When a wood particle is first inserted into the reactor, the particle-surface temperature rises rapidly, but the reflection from the reactor wall dominates the particle-surface radiance. It was observed that the particle surface was bright and then became black very soon. With Eq. 14 established for blue and red channels, together with green and red channels, surface temperature and emissivity of poplar particles in the single-particle reactor were calculated after the particle became black using particle pyrolysis videos taken by three cameras. An average particle surface emissivity of about 0.99 was obtained for the particle, even though a typical wood particle emissivity of 0.85 is widely used. This might be explained by the surface composition change due to biomass devolatilization: char was formed on the surface almost immediately after being exposed to the high-temperature furnace. Usually char has very high-emissivity. The camera-measured particle-surface temperatures as functions of time appear in Figure 18, compared with thermocouple- results. Three cameras were used to record images for the whole process since a single camera does not have enough dynamic range, with each camera set at different aperture size and exposure time. An uncertainty of about 100 K existed for the thermocouple measurements due to measurement difficulty (contact resistance, heat conduction along wires, effect of the scored surface, etc.). A single-particle combustion model[13] was also used to model the particle temperature, with predictions shown in Figure 18.

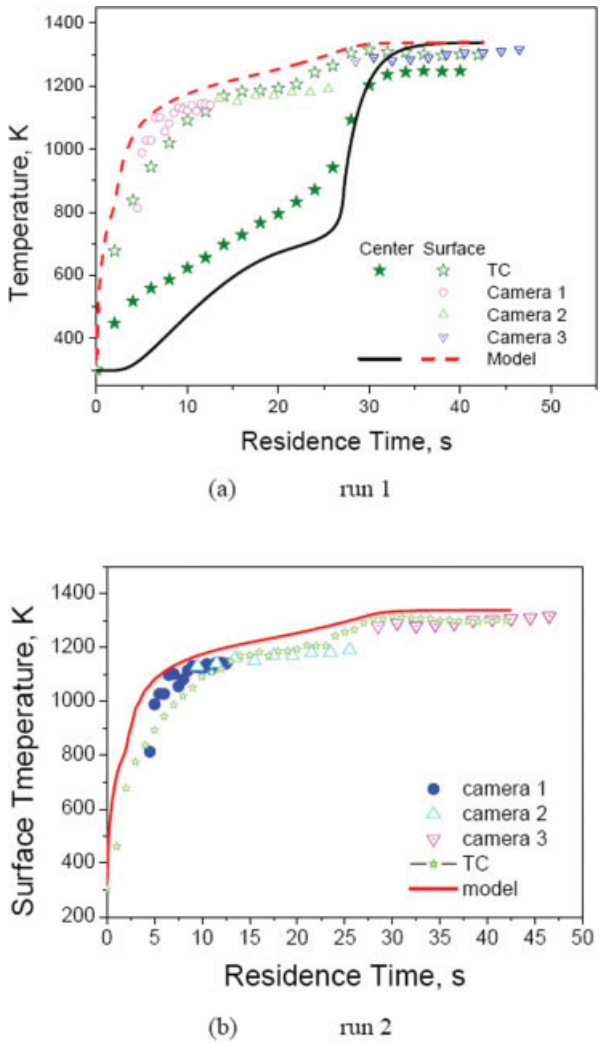


**Figure 18. Particle surface temperature comparisons during pyrolysis in nitrogen, (particle dia. = 9.5 mm, Tw = 1,373 K, Tg = 1,050 K).**

[Color figure can be viewed in the online issue, which is available at www.interscience.wiley.com.]

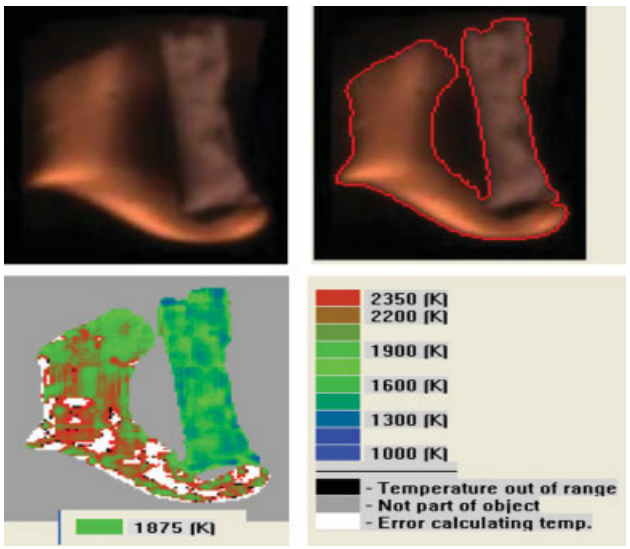


**Figure 19. Char particle surface temperature and flame temperature map during particle devolatilization process, (particle diameter = 9.5 mm, particle aspect ratio = 4.0, Tw = 1,273 K, Tg = 1,050 K).**

[Color figure can be viewed in the online issue, which is available at www.interscience.wiley.com.]

### *Particle-surface temperature and flame temperature during combustion*

Temperatures of a poplar particle surface and the surrounding flame measured dynamically when burning in the single-particle reactor appear in Figure 19. When calculating the flame temperature, soot absorption was ignored and gray body emission was assumed. Even though the flame (the large region to the left of the particle) reaches a fairly high temperature (over 2,300 K) due to the volatile combustion around the particle, the particle itself still stays at a low-temperature (1,400 – 1,700 K) mainly caused by the effects of outgassing and possibly endothermic decomposition reactions occurring in the particle. In the thermal images, some regions are marked as error since the pixel was saturated and accurate temperatures could not be obtained.

The flame temperature as a function of time for a particle burning in the single-particle reactor compared with thermocouple measured data and model predictions appear in Figure 20. In this case, the flame temperature measurement thermocouple was placed right next to the particle surface (about 1-2 mm) instead of being embedded in the particle, and it failed to measure the flame temperature after devolatilization. The transition point captured by the modeling results represents the transition from devolatilization to char oxidation of the particle during combustion process.

When a sawdust particle is traveling and burning in an entrained-flow reactor, the particle is usually covered by the

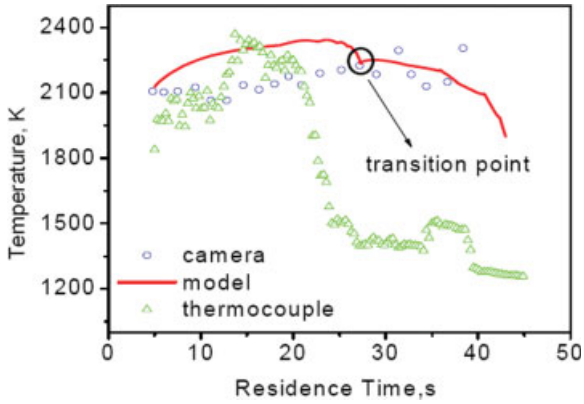


**Figure 20. Flame temperature comparison during a near-spherical particle combustion in air, (particle diameter = 9.5 mm, Tw = 1273 K, Tg = 1050 K).**

[Color figure can be viewed in the online issue, which is available at www.interscience.wiley.com.]

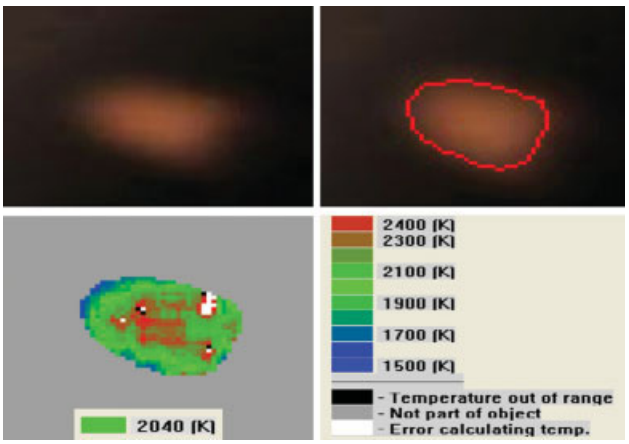


**Figure 21. Temperature map of sawdust particle in air in entrained-flow reactor, (particle diameter = 0.3 mm, Tw = 1,312 K, Tg = 1,124 K).**

[Color figure can be viewed in the online issue, which is available at www.interscience.wiley.com.]

flame formed next to it. Figure 21 maps flame temperature distribution back onto the image taken for a particle burning in the entrained flow reactor. The average flame temperature is about 2,040 K. This image is not as sharp as a stationary particle image and the edge area signal intensity is relatively low, which could potentially cause measurement errors in the edge area.

### *Char particle surface temperature during char burning*

A 3-D char particle-surface temperature map results from simultaneously taking three images of a single particle from three orthogonal directions. With the three images, 2-D particle-surface temperature distributions were calculated in each image. Then the temperature data were mapped to the surface of a 3-D particle-shape model reconstructed using the algorithm developed by Lu et al.[14] Results are shown in Figure 22.

Results show that the particle surface temperature is not uniform and obvious gradients exist. Both the particle geometry and bulk-gas-flow direction contribute to the nonuniform particle-surface temperature and gradients. Bulk gas flows upward. Both plane XZ and plane ZY face to the flow direction but plane XY is somehow parallel to the flow direction. This dramatically affects the surface-reaction rate and further influence the particle-surface-temperature distribution.

Char particle-surface temperature as function of time during the char burning process with the multicolor band camera pyrometer compared with thermocouple measured data and model predictions appears in Figure 23. Results show that the camera measured data are higher than predicted or thermocouple measured values. There is reason to believe that measured values may be higher than predicted by models, which do not account for 2- and 3-D effects caused by flames observed during char burning.

The images from such cameras reveal details of particle combustion that previously escaped quantitative measurement. For example, Figure 24 illustrates spatially resolved temperature and emissivity data from a burning black liquor particle in the early stages of char burning in which gases approach the particle from the bottom. The temperature data show large spatial differences in surface temperatures. Notably, a blow hole evident in the particle has a very low-temperature, presumably attributable to minimal oxygen access to the surface. However, the same blow hole shows a significantly higher emissivity than most of the particle surface, presumably because of the cavity radiation nature of such a surface depression. Black liquor contains high-concentrations of sodium salts that have relatively low-emissivity (typically around 0.15-0.2) whereas char emissivity's are high (0.85–

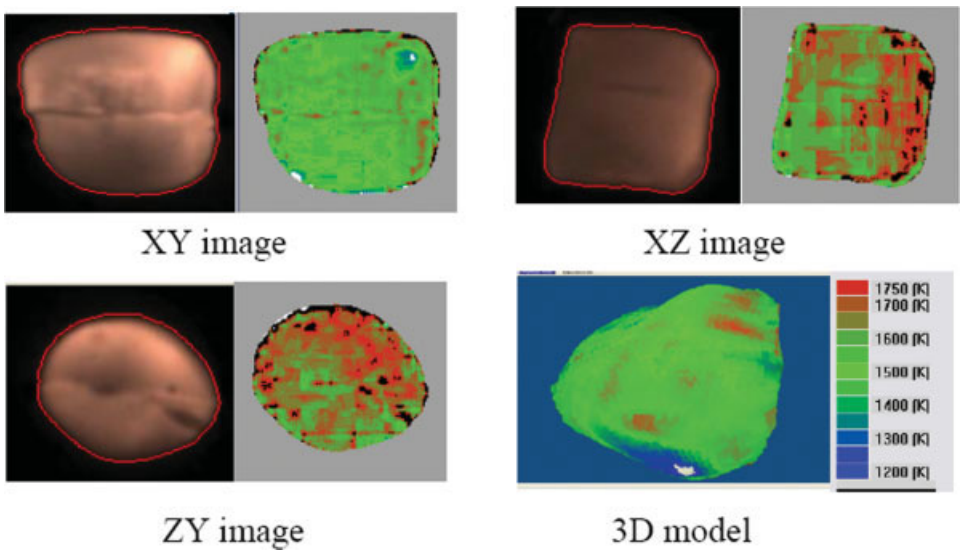


**Figure 22. 3-D particle-surface temperature map of a burning char particle, (particle diameter = 9.5 mm, Tw = 1,273 K, Tg = 1,050 K).**

[Color figure can be viewed in the online issue, which is available at www.interscience.wiley.com.]

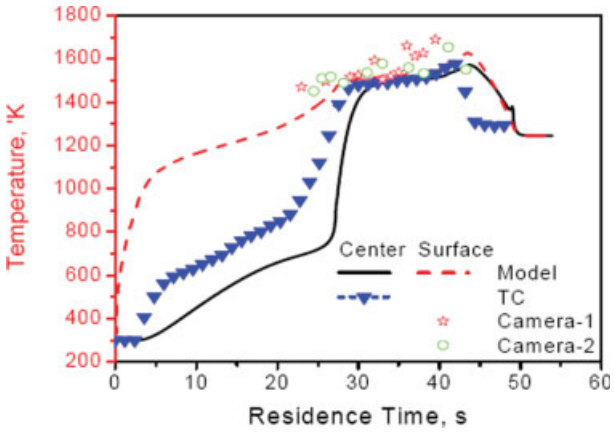


**Figure 23. Char particle-surface temperature as function of time during combustion in air, (particle diameter = 9.5 mm, Tw = 1,273 K, Tg = 1,050 K).**

[Color figure can be viewed in the online issue, which is available at www.interscience.wiley.com.]

0.99). The images indicate low emissivities on the windward edges of the particle and high emissivities on the leeward side of the image and along the left-side, which is protected somewhat from the oncoming gases by a surface protrusion. These differences presumably arise from more rapid char conversion and higher salt concentrations in the windward regions, consistent with the presumably thinner boundary layers and more rapid mass transfer. While the subject of this article is the development of this diagnostic, such images are rich in potential improved understanding of combustion behavior that is difficult to obtain by other techniques.

## Experimental Uncertainty

This section discusses the uncertainty of the experimental measurements. Two different sources of experimental uncertainty are considered: (1) errors associated with the measurement of the underlying parameters required to calculate the object surface temperature, (2) bias errors due to the violation of one of the fundamental assumptions. The uncertainties of the underlying measurements used to determine object surface temperature include three major components: sensor spectral responsivity, sensor uniformity, and calibration black body. The CCD sensor spectral responsivity curves were measured with monochromator and a high-pass filter. The uncertainty of the curves is less than ±2%. No data was collected to determine the sensor pixel uniformity, but the uncertainty was counted during the calibration. According to the black body spec, the uncertainty of the blackbody temperature is ± 1.5 C°. The total relative uncertainty caused by instruments (CCD camera and the blackbody) is ±3%, as shown in Figure 16.

Violation of one of the fundamental assumptions underlying the experimental technique represents the final source of experimental error. One potential violation is discussed: gray body emission. The color-band pyrometry assumes the particle surface emissivity is constant and independent of wavelength in the measurement range (400 – 1,100 nm). In this wavelength range, the char particle emissivity variation is usually less than 10%, which would results in a temperature measurement relative error of ±3% for single-color method. With the color-band technique discussed in this article, the temperature relative error will be less than ±3%. We use the worst case ±3% error in our overall uncertainty analysis.

The overall uncertainty of the color-band pyrometry temperature measurement technique is determined by combining in quadrature the relative uncertainty of the individual measurements (±3%), and the estimate of the experimental bias (±3%). The maximum overall relative uncertainty of the color-band pyrometry technique is ±4.5%.

If the spectral emissivity is known, the measurement accuracy of this technique can be dramatically increased. A CCD camera with high-sensitivity in near infrared (NIR) range will also increase the measurement accuracy.

## Conclusions

A multicolor band pyrometry algorithm, based on CMOS and CCD digital camera technology demonstrates dynamic, spatially resolved, temperature and emissivity measurements. Particle-surface temperature and flame temperature measurement results agree with thermocouple measurements and model predictions reasonably well. This new diagnostic pro-

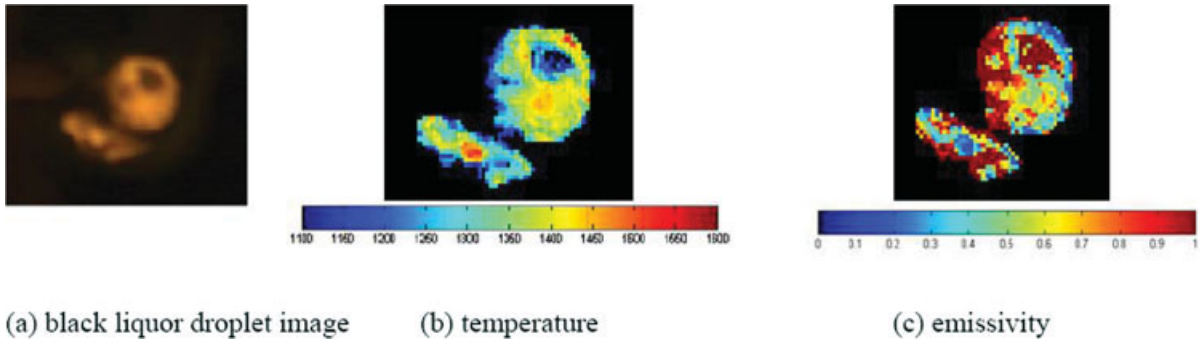


**Figure 24. Black liquor char particle images, temperature, and emissivity.**

[Color figure can be viewed in the online issue, which is available at www.interscience.wiley.com.]

vides pixel-by-pixel particle temperature and emissivity data from widely available and relatively inexpensive cameras. Depending on magnification, shutter speed, etc., useful temperature and emissivity data are obtainable at temperatures greater than about 750 K, with the lower limit based on signal intensity. Cameras more sensitive in the infrared produce useful data at lower-temperatures.

These noncontact particle temperature data compare reasonably well with both predictions and thermocouple measurements for both suspended and entrained-flow systems. The images allow 3-D reconstruction of particle temperature profiles that reveal large-surface temperature and emissivity differences.

## Acknowledgments

This investigation is supported by US Department of Energy (DOE)/ EE Office of Industrial Technologies.

## Notation

$a$ = pixel/cell area of CCD or CMOS sensor, $m^2$
$B$ = radiance, $W.Sr^{-1}.m^{-2}.nm^{-1}$
$C_1$, $C_2$ = constants in Planck's law
$d$ = working distance, m
$D$ = Lens diameter, m
$DN$ = digital number/pixel intensity, photon energy, J
$E$ = irradiance on sensor, $W.nm^{-1}$
$F$ = geometric configuration factor,
$g$ = camera gain value
$h$ = Planck's constant, $6.626 \times 10^{-34}$ $m^2.kg.s^{-1}$
$q$ = radiant energy flux, $J.m^{-2}$
$S$ = sensor sensitivity,
$Tg$ = gas temperature, K
$Tw$ = reactor-wall temperature, K
$X$ = area ratio of effective sensor over light source,

### *Greek letters*

$\lambda$ = wavelength, nm
$\sigma$ = Stefan-Boltzman constant, $W.m^{-2}.K^{-4}$
$\varepsilon$ = emissivity
$\tau$ = transmitter
$\Omega$ = solid angle, Sr
$t$ = camera exposure time, s

## Literature Cited

1. Mitchell RE, Niksa S. Temperature measurements of single pulverized-fuel particles by two-color pyrometry: II. particle burning behavior. In: Extended Abstracts, Spring Meeting - Electrochemical Society. San Francisco, CA: Electrochem Soc. Pennington, NJ; 1983.
2. Hernberg R, Stenberg J. Simultaneous in situ measurement of temperature and size of burning char particles in a fluidized bed furnace by means of fiberoptic pyrometry. *Combust Flame*. 1993;95:191–205.
3. Joutsenoja TS, Hernberg R. Pyrometric measurement of the temperature and size of individual combusting fuel particles. *Applied Optics*. 1997;36(7):1525–1535.
4. Murphy JJ, Shaddix CR. Influence of scattering and probe-volume heterogeneity on soot measurements using optical pyrometry. *Combust Flame*. 2005;143(1–2):1–10.
5. Fletcher TH. Time-resolved temperature measurements of individual coal particles during devolatilization. *Combust Sci Tech*. 1989;63: 89–105.
6. Tichenor DA, Mitchell RE, Hencken KR, Niksa S. Simultaneous in situ measurement of the size, temperature and velocity of particles in a combustion environment. In: 20th Symposium (International) on Combustion. The Combustion Institute; 1984.
7. Larsson A. Optical Studies in a DI Diesel Engine. *SAE Trans*. 1999;108(4):2137–2155.
8. Vattulainen J, Nummela V, Hemberg R, Kytola J. A system for quantitative imaging diagnostics and its application to pyrometric in-cylinder flame-temperature measurements in large diesel engines. *Meas Sci Tech*. 2000;11:103–119.
9. Bockaert V. Color Filter Array Sensor. 2003. [cited; Available from: http://www.dpreview.com/learn/?/key=color+filter+array.
10. Epix, Inc. Spectral responsivity of ZR32112 CMOS sensor. [cited; Available from: http://www.epixinc.com/products/ZR32112spectral-responsivity.pdf.
11. Sony, Inc. ICX285AQ CCD sensor spectral responsivity. 2005. [cited; Available from: http: //products.sel.sony.com/semi/PDF/ICX285AQ.pdf.
12. Siegel R, Howell J. Chapter Six - Radiation exchange in enclosures composed of black and/or diffuse-gray surfaces. In: *Thermal radiation heat transfer*. Taylor & Francis; 2002:207–267.
13. Lu H, Baxter LL. Effects of particle shape and size on biomass combustion. In: *Science in Thermal and Chemical Biomass Conversion*. Victoria, Vancouver Island, BC, Canada. 2004.
14. Lu H, Roberts W, Baxter LL. Effects of particle shape and size on biomass reactivity. In: Advanced Combustion Engineering Research Center Conference. Provo, UT; 2005.

*Manuscript received Jan. 18, 2008, and revision received Aug. 19, 2008.*